Eur. Phys. J. B **42**, 591–600 (2004)
DOI: 10.1140/epjb/e2005-00019-5

THE EUROPEAN PHYSICAL JOURNAL B

Traveling–stripe forcing of oblique rolls in anisotropic systems

S. Schuler, M. Hammele, and W. Zimmermann[a]

Theoretische Physik, Universität des Saarlandes, 66041 Saarbrücken, Germany

Received 30 July 2004
Published online 18 January 2005 –

Abstract. The effects of a traveling, spatially periodic forcing are investigated in a system with axial anisotropy, where oblique stripe patterns occur at threshold in the unforced case and where the forcing wavenumber and the wavenumber of stripes are close to a 2 : 1 resonance. The forcing induces an interaction between the two degenerate oblique stripe orientations and for larger forcing amplitudes rectangular patterns are induced, which are dragged in phase by the forcing. With increasing forcing velocity a transition from a locked rectangular pattern to an unlocked superposition of a rectangular and oblique stripe pattern takes place. In this transition regime, especially when the ratio between the wavenumber of the forcing and that of the pattern deviates from the 2 : 1 ratio, surprisingly stable or long living complex patterns, such as zig–zag patterns and patterns including domain walls are found. Even more surprising is the observation, that such coherent structures propagate faster than the stripe forcing.

PACS. 47.20.-k Hydrodynamic stability – 47.54.+r Pattern selection – 89.75.Kd Patterns

1 Introduction

External forcing of patterns is a powerful method for investigations of the response behavior of nonlinear patterns and of the inherently nonlinear mechanisms of self–organization. The effect of spatially periodic forcing on patterns has been investigated rather early in the context of thermal convection [1] and electroconvection in nematic liquid crystals [2,3]. Further on, the response of stationary patterns with respect to static periodic forcing in one or two spatial dimensions has been explored [2–9], as well as temporal forcing of traveling waves in hydrodynamics systems [10–12] and of temporally oscillating chemical reactions [13,14]. Recently, this branch of nonlinear science has been continued by a combination of spatial and temporal forcing in model systems [15–17], and by the introduction of light intensity modulation techniques in chemical reactions [13–20] and in electroconvection in nematic liquid crystals [21]. This suggests further interesting applications of spatiotemporal forcing, one of which is described in this work.

Here, the effects of a traveling, spatially periodic modulation of the control parameter,

$$M(x,t) = 2\hat{G}\cos[2(k_m x - \hat{\nu}t)], \tag{1}$$

are investigated in an anisotropic system, where oblique stripe patterns occur at the primary instability. Examples for such a system are thermal- or electroconvection in nematic liquid crystals [22–26]. In equation (1) $\hat{G}$ is the modulation amplitude, $2k_m$ is the modulation wavenumber and $\hat{\nu}$ determines the phase velocity $v_p = \hat{\nu}/k_m$ of the forcing. The effects of this forcing are analyzed in terms of symmetry adapted amplitude equations close to the threshold of the pattern forming instability.

The orientation of striped convection pattern in electroconvection or thermal convection in planarly aligned nematic liquid crystals may be either normal or oblique to the preferred direction [22–26]. The oblique stripe pattern at threshold can be written as follows [7,8,24]

$$\mathbf{u}(x,y,z,t) = e^{iq_c x}\left[A_1 e^{ip_c y} + A_2 e^{-ip_c y}\right]\mathbf{U}_0(z) + \text{c.c.}, \tag{2}$$

where c.c. means complex conjugate, $A_{1,2}$ are the complex amplitudes and $\mathbf{q}_c^O = (\pm q_c, \pm p_c)$ is the wavenumber. $\mathbf{u}(x,y,z,t)$ describes the physical variables, such as the spatiotemporal variation of the velocity field and the temperature modulation in convection or the optical birefringence of the pattern. $\mathbf{U}_0$ includes the variation of those fields across the fluid layer and for a vanishing wavenumber $p_c = 0$ the expression in equation (2) describes so–called normal stripes. Other anisotropic systems, such as for inclined layer convection [27–29] or Taylor-vortex flow [30–34], may be susceptible to similar effects as described in this work.

The case of a static and spatially resonant forcing with a modulation wave vector $2\mathbf{k}_m = (2k_m, 0) = (2q_c + 2\hat{q}_d, 0)$ nearly twice the x–component q_c of the wave vector characterizing the oblique rolls $\mathbf{q}_c^O = (\pm q_c, \pm p_c)$ has been studied in previous works [7,8]. Here $\hat{q}_d$ is the detuning and it has been found that spatially periodic forcing of the two

[a] e-mail: wz@lusi.uni-sb.de

degenerated oblique stripe states leads either to a rectangular pattern or to a superposition of a rectangular and an oblique stripe pattern. Here we investigate how the traveling stripe forcing given by equation (1) changes the bifurcation scenario of oblique stripes.

In Section 2 we describe equations for the two amplitudes $A_{1,2}$ of both oblique stripe states and the change of the threshold induced by the traveling stripe modulation is determined in Section 3. Two types of nonlinear solutions are calculated analytically in Section 4 and their linear stability properties are given in Section 5. A selected number of numerical solutions are presented in Section 6 and the article is finished with concluding remarks in Section 7.

2 Amplitude equations

In anisotropic systems, such as electroconvection (**EHC**) and Rayleigh-Bénard convection (**RBC**) in planarly aligned nematic liquid crystals, the concept of amplitude equations [35–37] is a very successful approach for the description of patterns close to their onset [24,26]. This approach relies on the basic assumption that the spatial variation of the amplitude $A(x,y,t)$ of a periodic pattern is small on the scale of the wavelength $2\pi/q_c$ or $2\pi/p_c$ of the pattern.

In the absence of external spatial modulations, the coupled equations for the amplitudes A_1 and A_2 of the two degenerated oblique stripe–states have been already derived in reference [24]. Generalizing these equations in a manner that includes the traveling and spatially periodic near $2:1$ resonant forcing of the control parameter, the following equations for the two amplitudes are obtained:

$$\tau_0\partial_t A_1 = \varepsilon A_1 + (\xi_1^2\partial_x^2 + \xi_2^2\partial_y^2 + 2a\xi_1\xi_2\partial_x\partial_y)A_1 + Ge^{2i(\hat{q}_d x-\hat{\nu}t)}A_2^* - g_1\left(|A_1|^2 + b|A_2|^2\right)A_1, \tag{3a}$$

$$\tau_0\partial_t A_2 = \varepsilon A_2 + (\xi_1^2\partial_x^2 + \xi_2^2\partial_y^2 - 2a\xi_1\xi_2\partial_x\partial_y)A_2 + Ge^{2i(\hat{q}_d x-\hat{\nu}t)}A_1^* - g_1\left(|A_2|^2 + b|A_1|^2\right)A_2. \tag{3b}$$

ε measures the distance from the threshold of oblique rolls and the frequency $\hat{\nu}$ is assumed to be of the order of the inverse relaxation time τ_0 of the pattern. ξ_1 and ξ_2 are the coherence lengths in x–direction and y–direction, respectively. The parameter a is a measure how the principal axes of the neutral surface are oriented with respect to the x and y–axis. The coefficient g_1 determines the amplitude of a stripe solution and together with the nonlinear interaction coefficient b, which is in most cases larger than one, it determines the amplitudes of rectangles and more complex patterns. The modulation function given by equation (1) breaks the translational symmetry along the x–axis, but one has still a translational invariance along the y–axis and invariance with respect to reflections $y \to -y$.

A rescaling of time and space coordinates, given by $t = \tau_0 t'$, $x = \xi_1 x'$, $y = \xi_2 y'$, yields a rescaled detuning $q_d = \hat{q}_d\xi_1$ and frequency $\nu = \hat{\nu}\tau_0$. Together with a rescaling of the amplitudes by $A_i = A_i'/\sqrt{g_1}$ $(i = 1,2)$ this results in the following two coupled equations:

$$\partial_{t'}A_1' = \varepsilon A_1' + (\partial_{x'}^2 + \partial_{y'}^2 + 2a\partial_{x'}\partial_{y'})A_1' + Ge^{2i(q_d x'-\nu t')}(A_2')^* - \left(|A_1'|^2 + b|A_2'|^2\right)A_1', \tag{4a}$$

$$\partial_{t'}A_2' = \varepsilon A_2' + (\partial_{x'}^2 + \partial_{y'}^2 - 2a\partial_{x'}\partial_{y'})A_2' + Ge^{2i(q_d x'-\nu t')}(A_1')^* - \left(|A_2'|^2 + b|A_1'|^2\right)A_2'. \tag{4b}$$

These coupled amplitude equations for a traveling spatially periodic $2:1$ forcing are of a similar form as the equations given in references [7,8].

In order to compare the results gained from the rescaled equations with real experiments, one has to determine experimentally the numerical values of τ_0 and $\xi_{1,2}$ of the considered system. A dimensionless velocity v' obtained for instance for a domain wall etc. in terms of equations (4) translates into the velocity $v = \xi_1/\tau_0\ v'$ in the real space of the periodic pattern $\mathbf{u}(x,y,t)$. This is important for comparison with real patterns. In Section 6 the solutions are also given in terms of the real field $\mathbf{u}$, which are determined by the amplitudes $A_{1,2}$ via equation (2) and for the related transformations we use in this work for reasons of simplicity $\tau_0 = \xi_{1,2} = g_1 = 1$, especially in Section 6.

The frequency ν and the detuning q_d in the exponential function of the forcing term may be removed by the simple transformation $A_{1,2}' = \bar{A}_{1,2}\exp[i(q_d x' - \nu t')]$, which transfers both parameters into the linear coefficients of the equation. Then one obtains the two coupled equations

$$\partial_{t'}\bar{A}_1 = [\varepsilon + i\nu + (iq_d + \partial_{x'})^2 + \partial_{y'}^2 + 2a(iq_d + \partial_{x'})\partial_{y'}]\bar{A}_1 - (|\bar{A}_1|^2 + b|\bar{A}_2|^2)\bar{A}_1 + G\bar{A}_2^*, \tag{5a}$$

$$\partial_{t'}\bar{A}_2 = [\varepsilon + i\nu + (iq_d + \partial_{x'})^2 + \partial_{y'}^2 - 2a(iq_d + \partial_{x'})\partial_{y'}]\bar{A}_2 - (|\bar{A}_2|^2 + b|\bar{A}_1|^2)\bar{A}_2 + G\bar{A}_1^*, \tag{5b}$$

which are investigated in this work.

3 Threshold

At first we investigate, how the threshold is modified by a traveling stripe forcing as given by equation (1). For this purpose we solve the linear parts of equations (5) by the ansatz

$$\bar{A}_1 = F_1\ e^{\sigma t' + i(Qx' + Py')}, \quad \bar{A}_2 = F_2\ e^{\sigma^* t' - i(Qx' + Py')} \tag{6}$$

with constant and complex coefficients F_1 and F_2. The solubility condition of the resulting two linear and homogeneous equations for $F_{1,2}$ gives the dispersion relation

$$\sigma = \varepsilon - \mathcal{A} \pm \sqrt{\mathcal{B}^2 + G^2 - \nu^2 - 2i\nu\mathcal{B}} \tag{7}$$

wherein the two abbreviations

$$\mathcal{A} = q_d^2 + Q^2 + P^2 + 2aq_dP, \tag{8a}$$
$$\mathcal{B} = 2Q(q_d + aP) \tag{8b}$$

are used. From the neutral stability condition $Re(\sigma) = 0$ one obtains the expression for the neutral surface $\varepsilon_0(Q, P)$

$$\varepsilon_0(Q,P) = \mathcal{A} - \sqrt{\tilde{M} + \sqrt{\tilde{M}^2 + \nu^2\mathcal{B}^2}}$$
$$\text{with} \qquad \tilde{M} = \frac{\mathcal{B}^2 + G^2 - \nu^2}{2}, \tag{9}$$

below which the basic state is linearly stable. The imaginary part of the dispersion relation at the surface $\varepsilon_0(Q, P)$ determines the frequency $\omega_0 = Im(\sigma)$ with

$$\omega_0 = -\frac{\nu\mathcal{B}}{\mathcal{A} - \varepsilon}. \tag{10}$$

Case $G^2 > \nu^2$

The first partial derivative of $\varepsilon_0(Q, P)$ as given by equation (9) vanishes at its extremal value at $Q = 0$ and it may be factorized as follows, $\partial_Q\varepsilon_0 = Q\ f(Q, P)$. The neutral surface has a minimum at $Q = 0$ if its second derivative $\partial^2\varepsilon_0/\partial Q^2|_{Q=0}$ is positive, which happens in some range for G beyond $|\nu|$ as described below. In this case for $Q_c = 0$ the neutral curve with respect to P is described by

$$\varepsilon_0(P) = q_d^2 + P^2 + 2aq_dP - \sqrt{G^2 - \nu^2} \tag{11}$$

and takes its minimum at $P_c = -aq_d$. So the threshold for $G > \nu$ and $Q_c = 0$ is finally given by

$$\varepsilon_c(G, q_d, \nu) = q_d^2(1 - a^2) - \sqrt{G^2 - \nu^2}. \tag{12}$$

However, the second derivative $\partial^2\varepsilon_0/\partial Q^2|_{Q=0,P=-aq_d}$ is only positive if the inequality

$$\frac{(G^2 - \nu^2)^{3/2}}{G^2} > 2q_d^2(1 - a^2)^2 \tag{13}$$

is fulfilled. The value G_L at the point L in Figures 1–3 is determined for the case that left hand side and right hand side of equation (13) are equal. As long as the minimum of the neutral curve is located at $Q_c = 0$, the corresponding frequency ω_c vanishes according to equation (10) and equation (8b).

However, $Q = 0$ does not correspond always to the minimum of the neutral surface. Below G_L, which is determined by equation (13), one has a negative second derivative $\partial^2\varepsilon_0(Q, P)/\partial Q^2|_{Q=0,P=-aq_d}$ and the critical wavenumber $Q_c \neq 0$ is nonvanishing. It has to be determined by a numerical minimization of $\varepsilon_0(Q, P)$ with respect to Q and P. For $G \to G_L$ and $G < G_L$ the critical wavenumber $Q_c \to 0$ tends continuously to zero and therefore the point L at G_L in Figures 1–3 is a so–called Lifshitz-point [22,23,38].

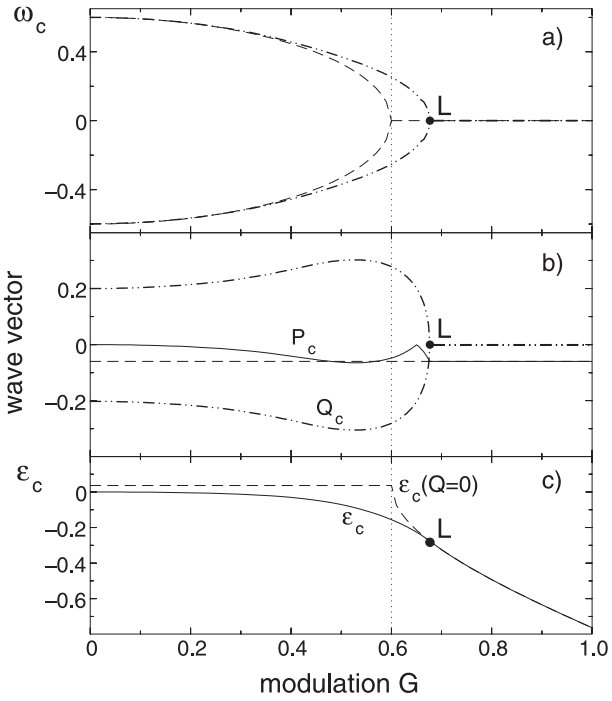

Fig. 1. This figure includes as a function of the modulation amplitude G the threshold ε_c in part (c), the critical wavenumbers Q_c and P_c in part (b) and the frequency ω_c in part (a) for the parameter value $a = 0.3$, a detuning $q_d = 0.2$ and a driving frequency $\nu = 0.6$. The dashed line in part (c) describes the analytical expression for the threshold $\varepsilon_c(Q = 0)$ as given by equation (12) for $G^2 > \nu^2$ and by equation (15) for $G^2 < \nu^2$, whereby the dashed lines in part (a) and (b) represent the respective analytical formulas for the position of the extreme value at $P_c = -aq_d$ ($Q_c = 0$) and the critical frequency $\omega_c = \pm\sqrt{\nu^2 - G^2}$. The two dash–dotted lines in part (b) describe Q_c as obtained by a numerical search for the extremum of the expression given by equation (9). The solid lines in part (b) and (c) represent the corresponding values of P_c and ε_c. The line types of the two numerical branches of ω_c (dash–dotted lines in a)) correspond to the two branches of Q_c. The dotted line separates the two regions $G < \nu$ and $G > \nu$.

Case $G^2 < \nu^2$

In this range the imaginary part of $\sigma(Q, P)$ is always finite and for $Q = 0$ the dispersion relation is of the simple form

$$\sigma = \varepsilon - q_d^2 - P^2 - 2aq_dP \pm i\sqrt{\nu^2 - G^2}. \tag{14}$$

The real part of this expression for σ becomes maximal at $P_c = -aq_d$ and for this value the neutral surface $\varepsilon_0(Q, P)$ following from $Re(\sigma) = 0$ takes its minimum at

$$\varepsilon_c(Q = 0, P_c = -aq_d) = q_d^2(1 - a^2). \tag{15}$$

The nonvanishing frequency at threshold is

$$\omega_c = \pm\sqrt{\nu^2 - G^2}. \tag{16}$$

However, similar as in the range $|\nu| < G < G_L$ above, the neutral surface takes in the whole range $G^2 < \nu^2$ its

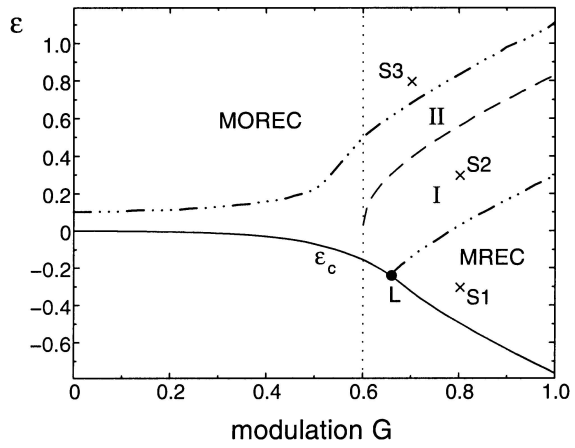

Fig. 2. The nonlinear analytical MREC solution given by equation (19) and the MOREC solution given by equation (21) are linearly stable for the parameter values $a = 0.5$, $b = 3$, $q_d = 0.2$, $\nu = 0.6$ in the range denoted by MREC and MOREC, respectively. Each of them becomes linearly unstable along the respective dash–dotted line. The solid line describes the threshold ε_c. The dotted line separates the two regions $G > \nu$ and $G < \nu$ and the dashed curve marks the continuous transition between these two types of nonlinear solutions.

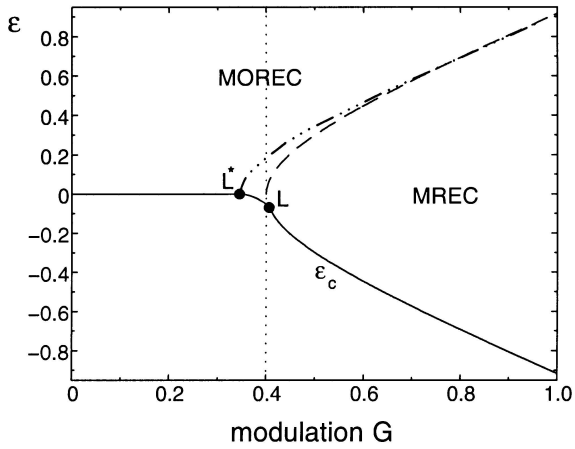

Fig. 3. Stability map for MREC and MOREC solutions in the case $q_d = 0$ for $a = 0.5$, $b = 3$ and $\nu = 0.4$. The solid line shows the threshold ε_c and the dotted line separates the two regions $G > \nu$ and $G < \nu$. For $\varepsilon > 0$ and $G > |\nu|$ along the dashed line, given by equation (22), a continuous transition between the MREC and MOREC solutions takes place. In the present case for $q_d = 0$ the transition coincides with the stability boundary for MREC. Below the dash–dotted line the MOREC solutions become linearly unstable with respect to small perturbations.

minimum at a finite value of $Q_c \neq 0$ and $P_c \neq -aq_d$, where both are obtained by a numerical determination of the minimum of the expression in equation (9).

Q_c and P_c as well as ε_c and ω_c are plotted as functions of G in Figure 1 and Q_c tends continuously to zero for $G \to G_L$, as described above. The G-dependence of the threshold and of the critical frequency ω_c at $Q = 0$, cf. equations (15) and (16), have been included for comparison and are described by the dashed lines.

The numerical results given in Figure 1 suggest $P_c \simeq 0$ and $\varepsilon_c \simeq 0$ for small values of the modulation amplitude G. In this case one approximately gets from the dispersion relation in equation (7) $\omega_c \simeq \pm\nu$ for the critical frequency and $Q_c \simeq \pm q_d$ for the corresponding critical wave vector in x-direction, which are described in Figure 1 by the dash-dotted lines. At threshold, the pattern propagates with a velocity $v \propto \nu - |\omega_c|$, as discussed in more detail in Section 4. In the limit $G \to 0$ this velocity vanishes and the solutions of equation (5) describe stationary stripes in y–direction ($P_c = 0$) with a wave vector that is shifted by q_d.

4 Analytical expressions for two nonlinear solutions

Analytical solutions of the nonlinear equations (5) are traveling waves as given by

$$\bar{A}_1 = F_1\, e^{i(Qx'+Py'-\Omega t')-i\psi},$$
$$\bar{A}_2 = F_2\, e^{-i(Qx'+Py'-\Omega t')}. \tag{17}$$

The two real and constant amplitudes $F_{1,2}$, the nonlinear frequency Ω and the relative phase shift ψ are determined by the real parts and the imaginary parts of the two equations

$$[\varepsilon - (q_d+Q)^2 - P^2 - 2a(q_d+Q)P + i(\nu+\Omega)]F_1 + G\, e^{i\psi}F_2 - F_1^3 - bF_2^2F_1 = 0, \tag{18a}$$

$$[\varepsilon - (q_d-Q)^2 - P^2 - 2a(q_d-Q)P + i(\nu-\Omega)]F_2 + G\, e^{i\psi}F_1 - F_2^3 - bF_1^2F_2 = 0. \tag{18b}$$

In the case $Q = 0$ and $P = -aq_d$ these equations may be solved analytically. In the range $G^2 > \nu^2$ one has a analytical solution with equal amplitudes $|F_1| = |F_2|$ and vanishing frequency Ω,

$$F_1^2 = F_2^2 = \frac{\tilde{\varepsilon} + \sqrt{G^2-\nu^2}}{1+b}, \quad \Omega = 0,$$
$$\sin\psi = -\frac{\nu}{G}, \tag{19}$$

where the abbreviation $\tilde{\varepsilon} = \varepsilon - q_d^2(1-a^2)$ has been introduced.

With unscaled coordinates this solution describes a moving rectangular pattern (**MREC**) in physical space

$$\mathbf{u} \propto F_1 \cos\left(k_x x - \hat{\nu}t - \frac{\psi}{2}\right)\cos\left(k_y y - \frac{\psi}{2}\right)\tilde{\mathbf{U}}_0(z, q_c, p_c)$$
$$\text{with}\quad k_x = q_c + \hat{q}_d, \quad k_y = p_c - a\hat{q}_d, \tag{20}$$

propagating with the phase velocity $v_p = \hat{\nu}/(q_c + \hat{q}_d)$ in x–direction that is identical with the phase velocity of the forcing.

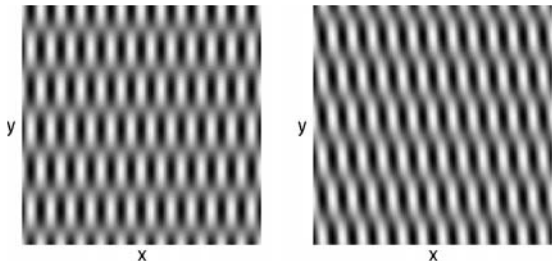

Fig. 4. Snapshots of one component of $\mathbf{u}(x, y, t)$ and for $q_d = 0$. The left part shows a snapshot of MREC comoving with the traveling stripe forcing and the right part shows one for a MOREC solution. For MREC the further parameters are $a = 0.5$, $b = 3$, $\varepsilon = 0.1$, $\nu = 0.4$, $G = 0.5$ and for MOREC two parameters were changed to $G = 0.6$ and $\varepsilon = 0.6$. For both cases $p_c = q_c/4$ has been used.

The second analytical solution has unequal amplitudes $F_1 \neq F_2$ and a finite frequency Ω with

$$\begin{aligned} F_{1,2}^2 &= \frac{\tilde{\varepsilon}}{2}(1 \pm \tilde{H}), \quad \Omega = -\tilde{H}\nu, \\ \sin\psi &= \frac{\nu}{G}\sqrt{1-\tilde{H}^2}, \\ \text{and} \qquad \tilde{H} &= \sqrt{1 - \frac{4G^2}{4\nu^2 + \tilde{\varepsilon}^2(1-b)^2}}\ . \end{aligned} \tag{21}$$

$\tilde{H}$ is always real for $G < \nu$. In the range $G > \nu$ it is only real if

$$\varepsilon \geq q_d^2(1-a^2) + \frac{2\sqrt{G^2-\nu^2}}{|1-b|} \tag{22}$$

holds. This solution with unequal amplitudes $F_1 \neq F_2$ describes in physical space a superposition of a moving rectangular and a moving oblique stripe pattern (**MOREC**), as can be seen by the representation in terms of $\mathbf{u}(x, y, t)$

$$\begin{aligned} \mathbf{u} \propto \tilde{\mathbf{U}}_0(z)\Big[& 2F_2 \cos\left(k_x x - \hat{\nu}t - \frac{\psi}{2}\right)\cos\left(k_y y - \hat{\Omega}t - \frac{\psi}{2}\right) \\ & + (F_1 - F_2)\cos\Big(k_x x + k_y y - (\hat{\nu} + \hat{\Omega})t + \psi\Big)\Big], \end{aligned} \tag{23}$$

with $\Omega = \hat{\Omega}\tau_0$. The first part in this expression corresponds to the rectangular contribution, which propagates in x–direction with the same velocity as the traveling stripe forcing, $v_x = \hat{\nu}/(q_c + \hat{q}_d)$. However, it propagates also in y–direction with a different velocity $v_y = \hat{\Omega}/(p_c - a\hat{q}_d)$, which tends to zero at the continuous transition line between MREC and MOREC solutions, i.e. along the dashed line in Figures 2 and 3, where both amplitudes become equal, $F_1 = F_2$. The second part in equation (23), the oblique stripe contribution, propagates in an oblique direction. However, close to the transition line between the MREC and MOREC solution the amplitude of the oblique stripe part of the MOREC solution tends to zero and the propagation in an oblique direction becomes in some sense irrelevant.

Typical snapshots of the MREC and the MOREC solution are shown in Figure 4 for $q_d = 0$ and $p_c = q_c/4$.

In the limit of small values of $G \to 0$, the MOREC solution becomes an oblique stripe pattern, where the propagation velocity to an oblique direction tends to zero, as indicated by the formula in equation (23) and the analytical expression for Ω given in equation (21). Roughly speaking, the MREC solutions are locked to the traveling stripe modulation and the MOREC solutions interpolates between these locked solutions and the unlocked ones in the limit $G \to 0$.

5 Linear stability of MREC and MOREC solutions

In certain parameter ranges, the nonlinear analytical solutions as given in Section 4 are linearly unstable with respect to small perturbations. The stable regime depends on the modulation amplitude, the control parameter, the wavenumber detuning and the propagation velocity of the forcing, as shown in this section. For this purpose the ansatz

$$\begin{aligned} \bar{A}_1 &= (F_1 + v_A(x', y', t'))\ e^{i(Qx' + Py' - \Omega t') - i\psi}, \\ \bar{A}_2 &= (F_2 + v_B(x', y', t'))\ e^{-i(Qx' + Py' - \Omega t')}, \end{aligned} \tag{24}$$

for any small perturbations with $|v_{A,B}| \ll |F_{1,2}|$ is chosen and equations (5) are linearized with respect to v_A and v_B. The resulting coupled equations for both fields are solved by the ansatz

$$\begin{aligned} v_A &= v_1\ e^{\sigma t' + i(Kx' + Ly')} + v_2\ e^{\sigma^* t' - i(Kx' + Ly')}, \\ v_B &= v_3\ e^{\sigma t' + i(Kx' + Ly')} + v_4\ e^{\sigma^* t' - i(Kx' + Ly')} \end{aligned} \tag{25}$$

with constant amplitudes v_i $(i = 1, 2, 3, 4)$. The resulting set of linear and homogeneous equations has solutions for nonvanishing amplitudes v_i only if the determinant of the coefficient matrix vanishes. This solubility condition gives an equation for the eigenvalue σ that may be determined mainly numerically. The stability boundary of the respective solution is then given by the condition $Re(\sigma) = 0$ after an extremalization with respect to K and L.

Case $q_d \neq 0$

For a finite wavenumber detuning $q_d \neq 0$ there are three major ranges beyond the threshold (solid line) in Figure 2. For $G > G_L$ one has above threshold stable moving rectangles (MREC) in a finite ε–range, which is bounded from above by the lower dash–dotted line. The width of this wedge like domain increases with G.

Beyond the upper dash–dotted line in Figure 2 MOREC solutions are linearly stable. In the limit $G \to 0$ the dash-dotted line terminates at the control parameter value $\varepsilon = q_d^2(1-a^2)b/|1-b|$ for $b < 3/2$ and at $\varepsilon = 3q_d^2(1-a^2)$ for $b > 3/2$, where both values of ε are determined analytically. Between both dash–dotted lines neither the MREC nor the MOREC are linearly stable. In this range more complex solutions, corresponding to finite values of Q, are preferred, as discussed in more detail in Section 6.

Limiting case $q_d = 0$

The threshold in this limiting case is described by the solid line in Figure 3. In a wide range $G < |\nu|$ the threshold vanishes, i.e. $\varepsilon_c = 0$, and beyond the point L ($G > G_L$) the threshold decreases according to equation (12) as a function of the modulation amplitude G as described by the expression

$$\varepsilon_c = -\sqrt{G^2 - \nu^2}. \tag{26}$$

However, in a finite range $G_{L^*} < G < |\nu|$ the threshold becomes negative and the wavenumber Q minimizing the threshold becomes finite. This is also the case in a small range $|\nu| < G < G_L$. In both cases, at the point L^* in Figure 3 at G_{L^*} and at the point L at G_L in the same figure the wavenumber Q decreases continuously to zero and therefore one has in addition to G_L also at G_{L^*} a Lifshitz–point.

The transition line between the two nonlinear solutions MREC and MOREC is given by equation (22) and it is described by the dashed line in Figure 3. It starts at $G = \nu$ and $\varepsilon = 0$ and coincides in a wide range with the upper linear stability limit for MREC solutions. The dash–dotted line in the same figure is the linear stability boundary for MOREC solutions. The solutions occurring between the dash–dotted and the dashed line are similar to the solutions found for the case $q_d \neq 0$ in the region II of Figure 2.

6 Numerical simulations

Here we investigate the nonlinear differential equations (5) by numerical simulations with a pseudo spectral method. If not stated otherwise, the range in the $x - y$ plane is a square with periodic boundary conditions and with a edge length of $40\lambda_0$, where $\lambda_0 = 2\pi/q_c$ is the wavelength of the pattern in x-direction, and ten grid points have been used per λ_0. We focus especially on the behavior of the solutions in the parameter range where the analytical MREC and MOREC solutions are linearly unstable.

6.1 Special case $q_d = 0$

For a vanishing wavenumber detuning $q_d = 0$ the MREC and the MOREC solutions are linearly stable nearly everywhere in the $\varepsilon - G$ plane, besides a small region near $G \sim \nu$, as indicated by the stability diagram in Figure 3. In Figure 4 snapshots of both solutions in their respective stable ranges are given in terms of a component of the real field $\mathbf{u}(x, y, t)$, which is determined by the amplitudes $A_{1,2}$ via equation (2) with the ratio $q_c/p_c = 4$. The edge length of each section is nearly one third of the total size of the system. The MREC solutions are locked in a frame comoving with the traveling stripe forcing and parts of the MOREC solutions travel slower and in a different direction according to equation (23) (see also the discussion behind this equation).

There is a continuous transition between a MREC and a MOREC, as shown analytically in Sections 4 and 5. This is also confirmed by numerical simulations for $q_d = 0$, where the simulation has been started in the MREC range of Figure 3 with a solution given by equation (19) and followed by an continuous increase of the control parameter up to the MOREC range in Figure 3.

Beyond the dash–dotted line in Figure 3, the MOREC solutions are linearly stable for $q_d = 0$ and by decreasing the modulation amplitude G the amplitude of one of the two modes A_i decreases too. While the MREC solutions are locked to the traveling stripe forcing the MOREC become more and more unlocked by decreasing the modulation amplitude G, being in agreement with the analytical results above.

6.2 General case $q_d \neq 0$

In the more general case we investigate the effects of a deviation q_d from the $2:1$ ratio between the spontaneous wavenumber q_c and the modulation wavenumber $2k_m$, i.e. $2k_m = 2(q_c + \hat{q}_d)$. In this case one expects a richer variety of solutions of equations (5), especially in the transition range between MOREC and MREC solutions.

Solutions in the range of stable MREC in Figure 2

In the MREC range of Figure 2 the comoving and locked rectangles, given by equations (19) and (20), are linearly stable. An example of this solution is shown in Figures 5a, c and e for parameters corresponding to the point S1 in Figure 2. Starting with random initial conditions this analytical solution is always the attracting one in the MREC parameter range in Figure 2. The corresponding field $\mathbf{u}(x, y, t)$ has the wavenumber $q_c + (q_d + Q)/\xi_1$ in x–direction and a wavenumber $p_c + P/\xi_2$ in y–direction with $Q = 0$ and $P = -aq_d$ on the level of the amplitude function $\bar{A}_i(x', y', t')$, which is shown in Figure 5c. In part (a) of this figure a section of a snapshot of this MREC pattern is shown in terms of $\mathbf{u}(x, y, t)$. Part (e) shows that the Fourier amplitudes of the two amplitudes $\bar{A}_1$ and $\bar{A}_2$ of the MREC pattern have the same modulus.

Solutions in the range of stable MOREC in Figure 2

A MOREC pattern as given analytically by equation (21) and by equation (23) has amplitudes $\bar{A}_{1,2}(x', y')$ that are periodic in y–direction with the wavenumber $P = -aq_d$ and constant along the x–direction, i.e. $Q = 0$. This pattern is also linearly stable in the range denoted by MOREC in Figure 2. However, MORECs are only stable with respect to tiny perturbations. Starting in simulations of equations (5) with a MOREC solution that is superposed by larger, but still small perturbations, then the MOREC pattern with wavenumber $Q = 0$, $P = -aq_d$ becomes unstable and solutions with wavenumbers $Q \neq 0$ and $P \neq -aq_d$ are preferred, similar as for the example shown in Figure 5d.

Starting a simulation of equations (5) with random initial conditions, long living transients occur that include a

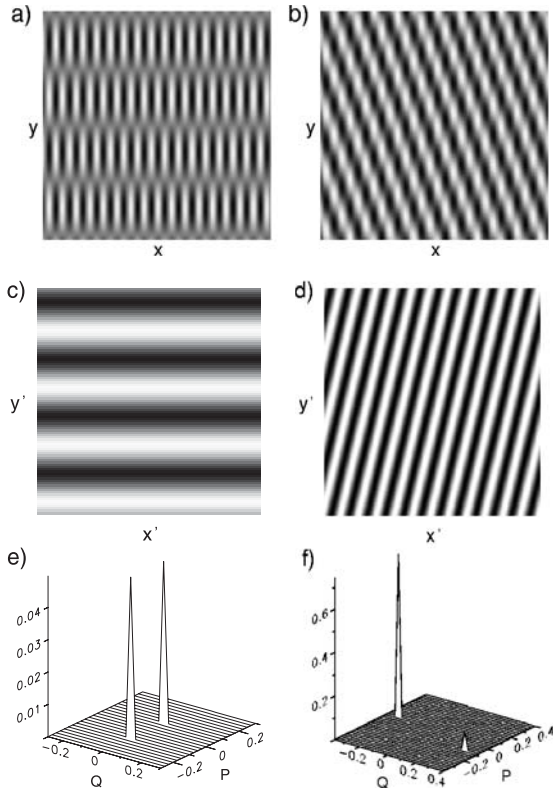

Fig. 5. The three parts (a), (c) and (e) describe a stable solution in the MREC region, as obtained after starting simulations with random initial conditions for the parameters $a = 0.5$, $b = 3$, $q_d = 0.2$, $\nu = 0.6$, $G = 0.8$, $\varepsilon = -0.3$. Part (c) shows the sum $\mathrm{Re}(\bar{A}_1 + \bar{A}_2)$, which is periodic in y-direction with a wavenumber $P = -aq_d$. Part (e) is the power spectrum of it and in part (a) a snapshot of this MREC is given in terms of $\mathbf{u}_i(x, y, t)$ with $p_c = q_c/4$, cf. equation (20). Parts (b), (d) and (f) give the respective results for a MOREC solution after starting with random initial conditions for modified values $\varepsilon = 0.8$ and $G = 0.7$. Part (d) shows the real part of $\bar{A}_1 + \bar{A}_2$, part (f) the power spectrum of it and the top part gives $\mathbf{u}_i(x, y, t)$ according to equation (23) with $p_c = q_c/2$.

larger number of defects, where most of them are annihilated in the course of time. Such a transient is shown in Figure 6, which includes two remaining defects. Near the defects, the typical MOREC pattern of oblique rolls with a superimposed rectangular structure is deformed by a kind of interstitial lattice line with endpoints at the two defects. Both defects will annihilate each other soon after the snapshot in Figure 6 and finally a state of oblique stripes is reached, similar to that one given in Figure 5d, but now with $|Q| \sim 0.3$ and $|P| \sim 0.1$. It is remarkable that $|Q| \sim 0.3$ is larger than the detuning q_d.

After starting with random initial conditions in the MOREC range of Figure 2 our simulations never terminate in a final state with wavenumber $Q = 0$, $P = -aq_d$ for the MOREC solution. Obviously, states with finite wavenumbers $Q \neq 0$ and $P \neq -aq_d$, where the specific values of Q and P depend on the parameters, have a much larger basin of attraction than the analytical MOREC solution with $Q = 0$, $P = -aq_d$. The moduli of the two

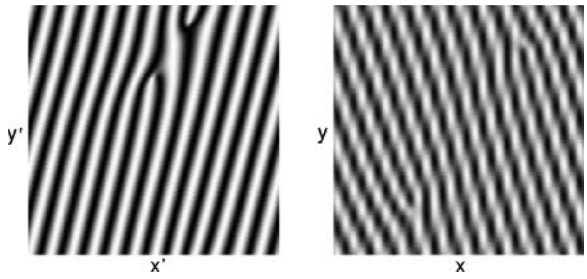

Fig. 6. The left part shows $Re(\bar{A}_1 + \bar{A}_2)$ for a transient state including a defect pair that is obtained in simulations started with random initial conditions and for parameters corresponding to the point S3 in the MOREC range in Figure 2, i.e. $a = 0.5$, $b = 3$, $q_d = 0.2$, $\nu = 0.6$, $G = 0.7$, $\varepsilon = 0.8$. In the right part a component of the corresponding real field $\mathbf{u}(x, y, t)$ is plotted in the neighborhood of the defect pair with $p_c = q_c/2$.

amplitudes A_1 and A_2 of such a MOREC solution differ remarkably for the parameters used for example in Figure 5d, as indicated in part (f) of the same figure.

In the region of linearly stable MOREC solutions in Figure 2, solutions that include domain walls also persist over a long time. Often there are pairs of straight domain walls parallel to the y–direction that propagate in terms of $\bar{A}_{1,2}$ slowly in the x–direction. A transformation to the spatially periodic pattern $\mathbf{u}(x, y, t)$ changes the phase velocity of the periodic pattern, but the velocity of the domain wall is the same in both representations. For example for a modulation amplitude of $G = 0.4$, a control parameter $\varepsilon = 0.4$ and all other parameters as in the right part of Figure 5, a simulation resulted in a state of the system with two nearly equally sized domains, where the domain boundaries are parallel to the y–direction and move in x–direction with a velocity of about 10% of the forcing velocity $v_p = \hat{\nu}/(q_c + \hat{q}_d)$ in unscaled units that corresponds in our example with $\xi_1 = 1$ and $\tau_0 = 1$ also to the velocity in scaled units of length and time $v_p' = \nu/(q_c + q_d)$. There are also solutions with domain walls parallel to the x–direction, but without any evidence for a movement of the domain walls perpendicular to their orientation.

Nonlinear solutions in region I of Figure 2

The MREC solution as given by equation (19) and with the wavenumber $Q = 0$ and $P = -aq_d$ is linearly unstable in range I of Figure 2. Starting in this range numerical simulations of equations (5) with random initial conditions one usually reaches states that include at intermediate stages domain walls as shown for example in Figure 7. Such domain walls move perpendicular to their orientation and very surprisingly, the propagation velocity of this domain wall in Figure 7 propagates 1.2 times as fast as the velocity v_p of the traveling forcing. Remember that we have with $\xi_1 = 1$ and $\tau_0 = 1$ the same velocity in scaled and unscaled units $v = \xi_1/\tau_0$ $v' = 1.2v_p$. During the course of time such domain walls as shown in Figure 7 may annihilate each other and the final state may consist of oblique stripes, similar as in Figure 5d.

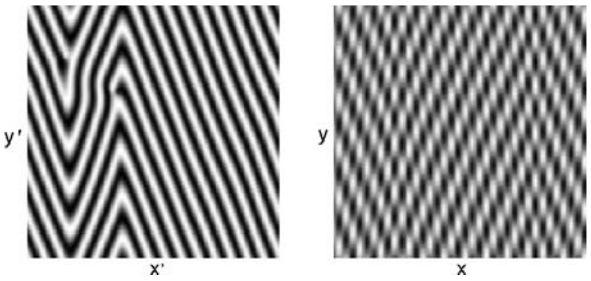

Fig. 7. The left part shows $Re(\bar{A}_1 + \bar{A}_2)$ as obtained by simulations of equations (5) after starting with random initial conditions for parameters at the point S2 in Figure 2, i.e. $a = 0.5$, $b = 3$, $q_d = 0.2$, $\nu = 0.6$, $G = 0.8$, $\varepsilon = 0.3$. The right part shows $\mathbf{u}_i(x, y, t)$ in a region near the lower left corner of the system including the two domain walls. This pattern is an intermediate transient that evolves further to a rather stable zig-zag pattern shown in Figure 8a.

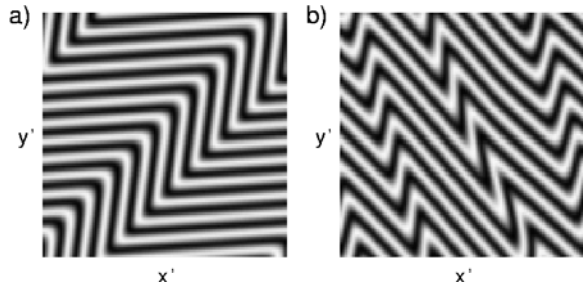

Fig. 8. The figure shows $Re(\bar{A}_1 + \bar{A}_2)$ of two stable solutions obtained in simulations for the same parameters as in Figure 7 but in part (b) for a different initial solution. The resulting zig-zag like final state in (b) has evolved from a slightly perturbed and inclined stripe pattern with the wave vector $(Q, P) = (0.05, -0.1)$, whereas the pattern in part (a) evolved from that in Figure 7.

Sometimes one may end up with a stable final state that is composed of two regions with different stripe orientations, similar to that in Figure 7. However, more often patterns as in Figure 7 occur only as a transient on the route to other stable complex patterns that are similar in the long time limit to the two examples in Figure 8. In both examples the domains move with a velocity of about 1.5 v_p also faster than the periodic forcing.

One component of the field $\mathbf{u}(x, y, t)$, corresponding to the stable solution in Figure 8a, is shown in Figure 9, whereby $p_c = q_c/2$ has been used during the transformation. The snapshot in Figure 9 covers the lower half of the area shown in Figure 8a. Similar to the case of the stable MREC solutions, the nearly horizontal stripes in the amplitude representation in Figure 8a generate a MREC–like pattern for the **u**–field. Due to the small deviation from exact horizontal stripes in Figure 8a, these are not perfect rectangles and they are slightly inclined. In the bulk of the horizontally striped region, the wave vectors and the phase velocity of the **u**–field nearly coincides with that of the exact MREC solutions.

The vertical striped range in Figure 8a transforms into a MOREC–like structure for the **u**–field, whose velocity

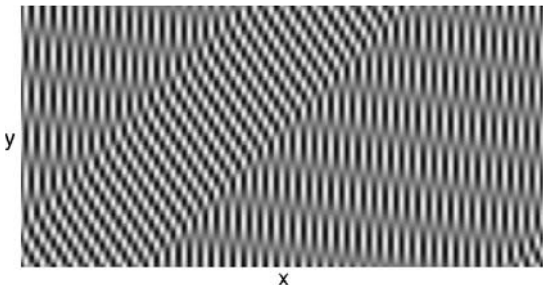

Fig. 9. The figure shows $\mathbf{u}_i(x, y, t)$ in a range corresponding to the lower half of the system shown in Figure 8a.

differs from that of the MREC–like pattern. As mentioned above, the boundaries of this MOREC–like region move synchronous with a larger velocity in x–direction than the inclined rectangles that are locked to the phase velocity of the periodic forcing.

For the parameters as in Figure 7, the time evolution of the spatially averaged quadratic modulus of the amplitudes, $\int dx'dy' \; |A_i(x', y', t')|^2$, is shown in Figure 10a. At the time marked with c in Figure 10a the snapshot that is shown in Figure 7 has been taken. This averaged quantity $\int dx'dy' \; |A_i(x', y', t')|^2$ is a measure for the global dynamics of a pattern and for the parameters as used in Figures 7 and 8 it becomes constant for long times, as can be seen in Figure 10a. The pattern corresponding to this constant behavior at this plateau in Figure 10a is the zig-zag pattern shown in the left part of Figure 8. This constant behavior is a strong indication for the surprising stability of the zig-zag pattern in Figure 8a. In the case of a static forcing, this pattern is unstable, i.e. it is only stabilized in region I by a finite forcing velocity. Actually, the simulations shown in Figure 10a have been continued up to $t' = 8 \times 10^4$ without any change of the constant behavior of $\int dx'dy' \; |A_i(x', y', t')|^2$ for the zig-zag pattern.

The time evolution of $|A_1(x'_0, y'_0, t')|^2$ at a fixed spatial point (x'_0, y'_0) is shown in part (b) and part (c) of Figure 10 at the times marked by b and c in part (a) of the same figure. Both curves indicate that the overall periodicity is determined by the propagating velocity of one of the domain walls. However, while the signal in Figure 10c, corresponding to the pattern in Figure 7, is already nearly periodic, the signal in Figure 10b, corresponding to a transient predecessor, shows stronger deviations from periodicity. This local signal shows a perfect periodicity for the zig-zag patterns in Figure 8a. The fact that one has a periodic behavior of $|A_1(x'_0, y'_0, t')|^2$, but a time–independent behavior in Figure 10a at long times, confirms that the pattern in Figure 8a moves as a whole everywhere with the same velocity and that it is stable. The periodic behavior of the local signal $|A_1(x'_0, y'_0, t')|^2$ as well as the constant behavior of $\int \; dx'dy' \; |A_1(x', y', t')|^2$ for the pattern in Figure 8a depends very much on the used periodic boundary conditions. For completeness it should be mentioned that the lifetime of the transient state of domain walls grows with the system size.

Instead of starting with a random initial solution, one can directly start with oblique stripe solutions, slightly

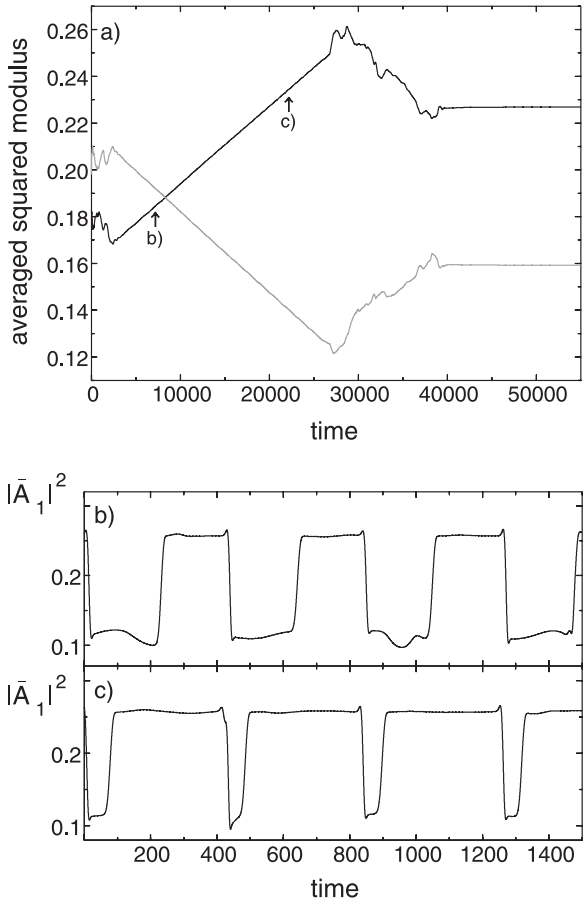

Fig. 10. Part (a) shows the time evolution of the spatially averaged amplitudes $\int dx'dy' |A_1(x', y', t')|^2$ (black) and $\int dx'dy' |A_2(x', y', t')|^2$ (gray). Close to the two times marked in part (a) by (b) and (c) the time–dependence of the squared modulus $|\bar{A}_1(x'_0, y'_0, t')|^2$ of each propagating pattern is shown in part (b) and part (c). The state in Figure 7 corresponds to the state in part (a) marked by (c). The pattern corresponding to the plateau at large times in part (a) is the zig-zag pattern in Figure 8a.

disturbed by adding a small random perturbation, and test their stability. In this case, the simulations show that only solutions with a not too small x-component Q of the wave vector will remain stable. For a starting solution with e.g. $Q = 0.05$ and $P = -0.1$ the right part of Figure 8 shows the resulting final state of the system. This state did not show further changes even in rather long lasting simulations and can also be considered as a stable pattern.

Many simulations in the region I suggest, that the final state is not unique and it depends very much on the initial conditions, as for instance the difference of the two patterns in Figure 8 shows. The difference between two final states resulting from two different realizations of the initial conditions may be even more drastic.

In region I in Figure 2, the system may also end up in a state of two equally spaced domains with walls parallel to the y-direction, filled with oblique stripes of different wave vectors, or in a pure state of oblique stripes.

Nonlinear solutions in the range II of Figure 2

Simulations starting with a slightly perturbed MOREC solution, cf. equation (21), as initial solution confirm the instability of these solutions in region II of the phase diagram in Figure 2. Starting with random initial conditions one often terminates in a state with two moving domain walls, which separate regions of oblique stripes, similar as in Figure 7a. In contrast to the case of unstable MREC solutions, here the width of these domains remains always constant and this state including domain walls is a stable one in this region. Furthermore, stable final states consisting of one type of oblique stripes in terms of $\bar{A}(x', y', t')$ are also possible. More complex stable patterns similar to that in in Figure 8 found in region I of Figure 2, have not been seen in region II.

7 Summary and conclusions

In this work we have generalized an earlier investigation about the effects of spatially periodic static forcing on a stationary bifurcation to an oblique stripe pattern in anisotropic systems, cf. references [7,8]. Here we investigate, how a propagating spatially periodic forcing, as given by equation (1), acts on the bifurcation to oblique stripes. For this we have restricted our study to a forcing wavenumber $2k_m$ in x–direction, which is roughly two times as large as the wavenumber q_c in x–direction of the pattern, i.e. $2k_m = 2(q_c + \hat{q}_d)$. This corresponds to a 2 : 1 resonance, but allows a small detuning $\hat{q}_d$.

For fairly large modulation amplitudes we found at threshold moving rectangles (MREC), a snapshot of them is given in Figure 4. The MREC solution is locked to the forcing and propagates with the velocity of the periodic forcing along the x–direction, $v_p = \hat{\nu}/(q_c + \hat{q}_d)$. If the control parameter is increased further beyond threshold or if the velocity of the forcing is increased, a MREC pattern becomes unstable. If the wavenumber detuning $\hat{q}_d$ vanishes, there is a continuous transition to a moving superposition of rectangles and oblique stripes (MOREC), whereby in this case the propagation velocity does not coincide anymore with the forcing velocity. Moreover, with increasing values of the control parameter or decreasing values of the modulation amplitude, the propagation velocity of the MOREC decreases continuously.

For a finite detuning $\hat{q}_d \neq 0$ interesting and new stable complex patterns occur in the transition regime between MREC and MOREC patterns. These are for instance patterns that include stable domain walls or patterns where domain walls are coming and going during long lasting transients, which may finally terminate in periodic patterns but with $Q, P \neq 0$. Or they relax, especially in the range I of Figure 2, to zig–zag patterns such as shown for example in Figure 8. Zig-zag pattern of this type are very stable, as indicated in Figure 10, but they are unstable outside the range I in Figure 2 and they are also unstable for nonpropagating spatially periodic forcing. Therefore, such zig–zag patterns are a characteristic response behavior of oblique rolls with respect to a nearly 2 : 1 resonant

traveling forcing. Moreover, and an even more surprising behavior is the propagation velocity of such zig–zag domains. They propagate for the parameters as chosen in Figure 8 about 1.5 times as fast as the propagating stripe forcing.

The patterns as well as the various transition scenarios as described in this work are expected to be observable in experiments similar as in references [9,21] with a material as used in reference [23]. In spiral vortex flow [30–34] one has also two degenerated states at threshold with respect to a preferred direction. However, these are propagating states and are described by amplitude equations with complex coefficient [37]. Nevertheless a spatial periodic modulation in the direction parallel to the cylinder axis may give rise to similar and other interesting scenarios to be investigated in the future.

Interesting discussions with M. Hilt and F. Ziebert are very much appreciated.

References

1. R.E. Kelly, D. Pal, J. Fluid Mech. **86**, 433 (1978)
2. M. Lowe, J.P. Gollub, T. Lubensky, Phys. Rev. Lett. **51**, 786 (1983)
3. M. Lowe, B.S. Albert, J.P. Gollub, J. Fluid Mech. **173**, 253 (1986)
4. P. Coullet, Phys. Rev. Lett. **56**, 724 (1986)
5. P. Coullet, D. Repaux, Europhys. Lett. **3**, 573 (1987)
6. P. Coullet, D. Walgraef, Europhys. Lett. **10**, 525 (1989)
7. W. Zimmermann et al., Europhys. Lett. **24**, 217 (1993)
8. A. Ogawa, W. Zimmermann, K. Kawasaki, T. Kawakatsu, J. Phys. II France **6**, 305 (1996)
9. Y. Hidaka, T. Fujimura, N.A. Mori, S. Kai, Mol Cryst. & Liq. Cryst. **328**, 565 (1999)
10. I. Rehberg et al., Phys. Rev. Lett. **61**, 2449 (1988)
11. H. Riecke, J.D. Crawford, E. Knobloch, Phys. Rev. Lett. **61**, 1942 (1988)
12. D. Walgraef, Europhys. Lett. **7**, 485 (1988)
13. A.L. Lin et al., Phys. Rev. Lett. **84**, 4240 (2000)
14. A.L. Lin et al., Phys. Rev. E **62**, 3790 (2000)
15. C. Utzny, W. Zimmermann, M. Bär, Europhys. Lett. **57**, 113 (2002)
16. S. Rüdiger et al., Phys. Rev. Lett. **90**, 128301 (2003)
17. D.G. Miguez et al., Phys. Rev. Lett. **93**, 048303 (2004)
18. M. Dolnik, I. Berenstein, A.M. Zhabotinsky, I.R. Epstein, Phys. Rev. Lett. **87**, 238301 (2001)
19. I. Berenstein et al., Phys. Rev. Lett. **91**, 058302 (2003)
20. V.K. Vanag, I.R. Epstein, Phys. Rev. E **67**, 066219 (2003)
21. M. Henriot, J. Burguette, R. Ribotta, Phys. Rev. Lett. **91**, 104501 (2003)
22. W. Zimmermann, L. Kramer, Phys. Rev. Lett. **55**, 402 (1985)
23. R. Ribotta, A. Joets, L. Lei, Phys. Rev. Lett. **56**, 1595 (1986)
24. E. Bodenschatz, W. Zimmermann, L. Kramer, J. Phys. (France) **49**, 1875 (1988)
25. S. Kai, W. Zimmermann, Prog. Theor. Phys. Suppl. **99**, 458 (1989)
26. L. Kramer, W. Pesch, Annu. Rev. Fluid Mech. **27**, 515 (1995)
27. J.E. Hart, J. Fluid Mech. **47**, 547 (1971)
28. L.N. Shadid, R.J. Goldstein, J. Fluid Mech. **215**, 61 (1990)
29. K.E. Daniels, B.B. Plapp, E. Bodenschatz, Phys. Rev. Lett. **84**, 5320 (2000)
30. *The Couette-Taylor Problem*, edited by P. Chossat, G. Iooss (Springer, Berlin, 1994)
31. E.R. Krueger, A. Gross, R.C. DiPrima, J. Fluid Mech. **24**, 521 (1966)
32. H.A. Snyder, Phys. Fluids **11**, 728 (1968)
33. C.D. Anderek, S.S. Liu, H.L. Swinney, P.S. Marcus, J. Fluid Mech. **164**, 155 (1986)
34. C. Hoffmann, M. Lücke, A. Pinter, Phys. Rev. E **69**, 056309 (2004)
35. A.C. Newell, J.A. Whitehead, J. Fluid Mech. **38**, 279 (1969)
36. A.C. Newell, T. Passot, J. Lega, Annu. Rev. Fluid Mech. **25**, 399 (1992)
37. M.C. Cross, P.C. Hohenberg, Rev. Mod. Phys. **65**, 851 (1993)
38. W. Pesch, L. Kramer, Z. Physik B **63**, 121 (1986)